PAPER • OPEN ACCESS

Experimental analysis of a low controlling voltage tri-electrode MEMS electrostatic actuator for array applications

View the article online for updates and enhancements.

Experimental analysis of a low controlling voltage tri-electrode MEMS electrostatic actuator for array applications

Mehdi Allameh[1,*] ⓘ**, Yu Zhou**[1] ⓘ**, Tao Chen**[1]**, Dwayne Chrusch**[1]**, Byoungyoul Park**[2] ⓘ **and Cyrus Shafai**[1]

[1] Department of Electrical and Computer Engineering, University of Manitoba, Winnipeg, Canada
[2] Nanotechnology Research Centre, National Research Council Canada, Edmonton, Canada

E-mail: allamemm@myumanitoba.ca

CrossMark

Abstract

A tri-electrode electrostatic actuator with one moving microelectromechanical systems (MEMS) electrode and two stationary electrodes (tri-electrode actuator topology) is experimentally tested in this article. The stationary controlling (intermediate) electrode is perforated and below the moving MEMS electrode, and the common electrode is further below. Numerical simulations were performed to discover the most optimum tri-electrode design parameters to enable the best performance improvement compared to a conventional two electrode electrostatic actuator. A silicon-based moving MEMS electrode was designed with a relatively linear spring constant, and the controlling intermediate and primary stationary electrodes were fabricated on either side of a quartz substrate instead of free space to simplify their fabrication. The measurement results showed that the tri-electrode topology can control the displacement of the MEMS with a lower controlling voltage and with extended controllable range before pull-in instability, compared to the conventional actuator. Simulations and measurements showed the controlling voltage was decreased by 2.6 times smaller than the conventional actuator topology using a bipolar driven intermediate electrode, and the controllable deflection range before pull-in was elevated by 33%. This tri-electrode topology offers benefits for applications in need of arrays of electrostatic actuators such as deformable mirrors.

Keywords: MEMS, electrostatic actuator, FEM, pull-in effect, deflection range, controlling voltage

(Some figures may appear in colour only in the online journal)

---

* Author to whom any correspondence should be addressed.

1. Introduction

Adaptive optics (AO) technology has seen a considerable advance in the last few decades and is being employed in various fields, including but not limited to astronomy, microscopy, and vision science [1–6]. AO systems utilize a segmented mirror or a deformable mirror (DM) to correct an aberrated wavefront such as due to atmospheric turbulence [7–14]. DMs, as one of the main parts of an AO system, consists of two parts of a flexible reflective layer (mirror face sheet) and an array of actuators deforming the flexible surface located on the back of the reflective layer. There are various types of DMs technology, but the MEMS designs are more popular due to their potential for batch production and compact size [15–18]. Many MEMS actuators have been employed in manufacturing DMs [19–22], with the electrostatic actuator being one of the most popular due to its low steady-state power consumption and compact design. However, DMs with electrostatic actuators face pull-in instability [23], which limits the actuator deflection range, and leading to DMs being applied for lower stroke applications resulting weaker astronomical performance [17]. Increasing the initial gap spacing between the actuator's electrodes can help increase the deflection range, but the drawback is the need for a higher controlling voltage. Thus, deflection range and the controlling voltage of an electrostatic actuator are the two parameters that are necessary to be improved for enabling DMs with higher performance.

Aside from DMs, an electrostatic actuator with higher performance is advantageous for other types of applications such as high isolation MEMS switches and micro pumps. The potential for lower controlling voltage is specifically more advantageous when there is a need for arrays of actuators. For example, supplying hundreds or thousands of actuators with 100 V or more is very challenging since each single actuator requires a separate high voltage amplifier. There have been numbers of solutions for lowering the voltage; however, they are not specifically designed for arrays of actuators.

Several solutions have been reported to overcome the pull-in instability. Pre-stress structures were utilized to reduce the controlling voltage and increase the deflection range. Chiou and Lin [24] used a pre-stress comb-drive actuator to solve the pull-in instability. The actuator does not have the pull-in instability problem, and it has a longer displacement range and low voltage. However, the actuator's initial lift highly depends on the residual stress and manufacturing steps, so a possible minor change in the material thickness can alter the designed lift. Furthermore, post-heat treatment is always needed to elevate the lift to a desired value. In [25], Chu *et al* also used the residual stress to bend up a radio frequency MEMS switch and control the gap between electrodes by gradient stresses. The switching voltage is small due to the controlled small gap between electrodes. However, the actuator's characteristics highly depend on the residual stress and fabrication steps characteristics. Using nonlinear springs is another way to extend the actuator deflection range. In [26], nonlinear springs increased the travel range by reducing the positive feedback. However, nonlinear springs can have the problem of increasing the controlling voltage. Offset electrode designs [27–30]

are another common reported method to improve the deflection range. The offset electrode configuration also reduces the pull-in instability. However, the overall size of the MEMS is larger due to the adjacent electrodes. Atik *et al* introduced an electrostatically actuated MEMS micro-valve for flow manipulation in microfluidics. The moving electrode was a circular diaphragm opening and closing the fluid channel. One issue of this design is for having better leakage behavior, a thicker diaphragm is needed and as a result, a higher controlling voltage is required. This can be a serious problem as the regular pull-in voltage was as high as the average of 221 V [31]. Admassu *et al* built a parallel plate electrostatic micro-actuator with three spring-like x-beam configurations. Different springs were examined in each configuration, and it was shown that the serpentine spring is more flexible which results in a lower control voltage. However, for that configuration with serpentine springs, the required voltage is 128 V for only 9.89 μm of displacement [32]. Banerjee *et al* presented a low-cost and compact electrostatically actuated DM with an aperture size of 10 mm. Standard micro-machining techniques were used to build the device to reduce the fabrication cost. The maximum stroke of the DM is as high as 15 μm. However, a relatively high voltage of 375 V is needed [16].

In [33, 34], a novel tri-electrode topology was introduced to reduce the controlling voltage and increase the deflection range. In this topology, two stacked electrodes are used, forming a compact structure. The intermediate electrode is perforated, allowing a low voltage on this electrode to modulate the lower (primary) electrode's background electric field provided by a fixed voltage.

This paper presents experimental testing of a tri-electrode low voltage and large stroke electrostatic actuator. A silicon-based MEMS moving electrode is designed to implement the actuator topology. The MEMS electrode is supported by four serpentine springs and is placed over the perforated controlling intermediate electrode. The primary electrode is located under the intermediate electrode providing the background electrostatic force to be modulated by the controlling intermediate electrode. The primary electrode and intermediate electrode are separated by a quartz substrate to facilitate fabrication. First, the design, the parametric analysis, and simulations for the specific actuator and tri-electrode topology are presented. Finite element method (FEM) analyses are used to study the actuator performance and extract the resulted electrostatic forces applied by the controlling voltage. In sections 3 and 4, fabrication and experimental measurements are presented.

2. Design and parametric analysis

The conventional electrostatic actuators consist of one stationary electrode and one MEMS moving electrode, as shown in figure 1. There have been various designs for the moving platform and spring structure, however, a straightforward configuration can be a flat rigid silicon-based platform supported by micro-springs [35]. Due to the pull-in effect, the conventional electrostatic actuator snaps down after traveling one-third of the initial gap. This means that in order to increase the control
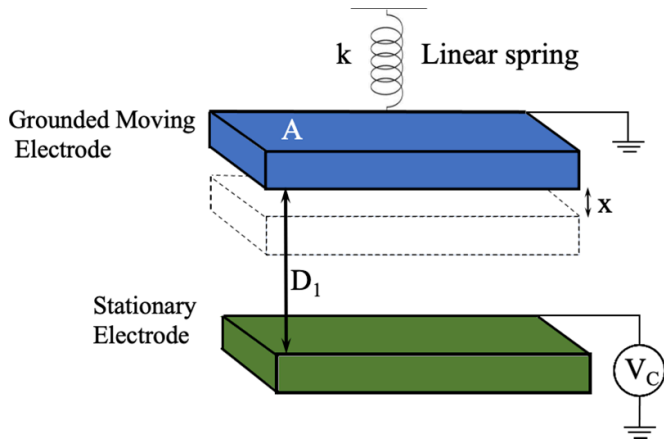
Figure 1. Conventional electrostatic actuator topology with one stationary and one moving (MEMS) electrode.
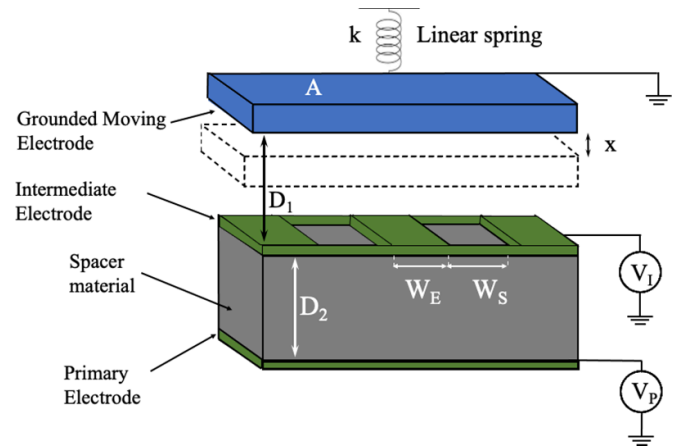

Figure 2. Tri-electrode actuator topology using two stationary perforated intermediate electrode and one solid primary electrode. The MEMS moving electrode is at D_1 distance from the intermediate electrode. W_S and W_E are the spacing and the electrode width of the intermediate electrode respectively.

range, a larger initial gap is required, which results in a larger controlling voltage.

2.1. Tri-electrode topology

The tri-electrode topology was already introduced and studied in [33] using FEM and restoring spring force method (RSFM). All the design parameters were investigated, and their influence on the actuator performance was reported. As shown in figure 2, there are two underlying stationary electrodes in the tri-electrode configuration compared to the conventional topology, which has only one stationary electrode. The perforated intermediate electrode controls the MEMS moving electrode. The bottom primary electrode sits further from the moving MEMS electrode. It provides a fixed background electric field to boost the attractive electrostatic force and compensate the smaller effective area of the intermediate electrode. Together these two electrodes, allow the perforated intermediate electrode to enable similar deflections as the conventional topology, but with a lower controlling voltage (V_I). In addition, the tri-electrode topology can provide a longer displacement before snap-down occurs, larger than the one-third of the initial gap of the convention actuator situation.

The design parameters to be considered in the tri-electrode actuator are the perforation size (W_E) and spacing (W_S) of the intermediate electrode, the separation of the MEMS moving electrode from the intermediate electrode (D_1), the separation of the intermediate electrode to the underlying primary electrode (D_2), and the fixed voltage on the bottom primary electrode (V_P). The tri-electrode performance varies depending on these various design parameters [33].

Figure 3 contrasts the performance of a conventional actuator, with an arbitrary tri-electrode system for the situation with design parameters $W_S = 2.5\,D_1$, $W_E = 0.83\,D_1$, $D_2 = 1.67\,D_1$, and $V_P = 4.37\,V_{\text{snap-down}}$. For the conventional actuator, snap-down occurs at $X_{\text{snap-down}} = 1/3\,D_1$ and at a voltage $V_{\text{snap-down}}$. The red crosses show the snap-down point where the actuator becomes unstable. In order to contrast the performance of the tri-electrode compared to the conventional
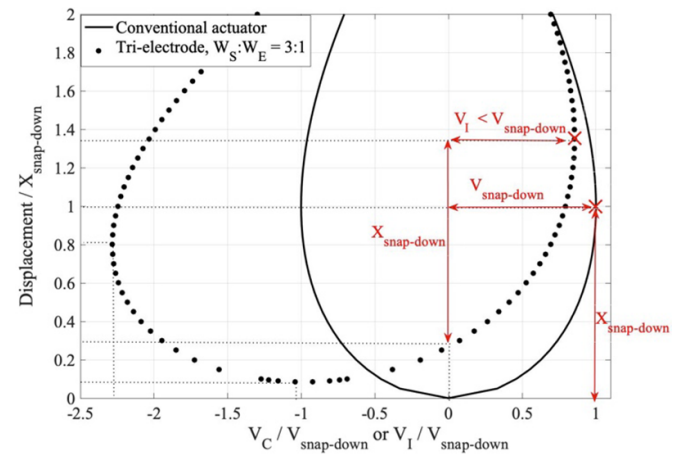

Figure 3. Displacement vs. controlling voltage (V_C or V_I) of the conventional topology (solid line) with D_1 gap spacing between the electrodes, and the tri-electrode topology (dotted line) with air between intermediate and primary electrodes when $D_2 : D_1 = 1.67$, $W_S = 2.5\,D_1$, $W_E = 0.83\,D_1$ ($W_S : W_E = 3 : 1$) and $V_P = 4.37\,V_{\text{snap-down}}$.

topology, the response curves in figure 3 are normalized with the conventional topology response curve characteristics.

As can be seen for this particular design, the tri-electrode controlling voltage (V_I) is smaller than the conventional controlling voltage ($V_{\text{snap-down}}$) by a factor of 1.25 for achieving the same deflection possible for the conventional actuators ($X_{\text{snap-down}}$). It should be mentioned that to enable this superior decrease in the needed controlling voltage V_I on the intermediate electrode, compared to the conventional actuator, the tri-electrode's bottom primary electrode is biased to a fixed voltage greater than that of $V_{\text{snap-down}}$ ($V_P = 4.37\,V_{\text{snap-down}}$). In the case of actuator array applications, the disadvantage of having one common larger voltage V_P on the bottom primary electrode is outweighed by the benefit of each individual actuator needing a smaller individual controlling voltage V_I.
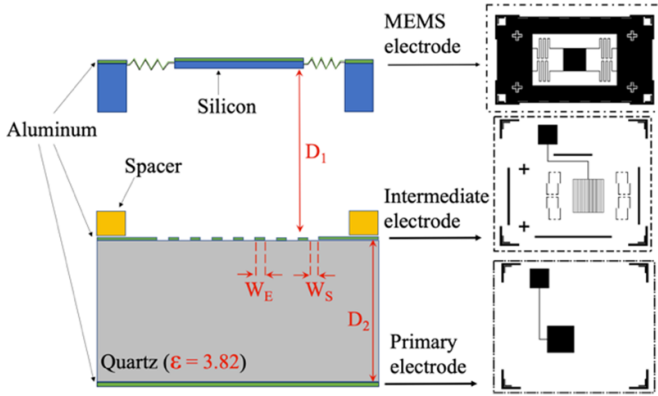
Figure 4. The schematic and the designed mask of the tri-electrode actuator using quartz ($\varepsilon_r = 3.82$) as spacer material between intermediate and primary electrodes.
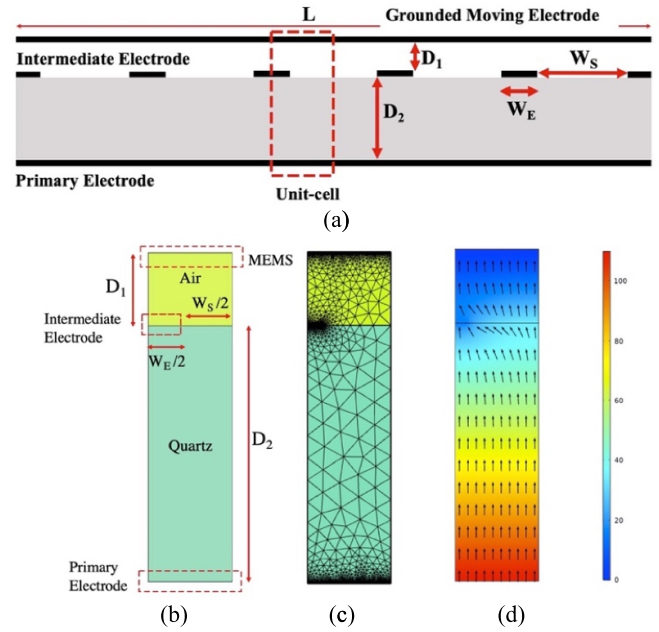

Figure 5. 2D cross-section of the tri-electrode topology. (a) Complete geometry. (b) Unit-cell parameters. (c) Mesh size for FEM analysis. (d) Potential distribution between electrodes when ($V_P = 120$ V).

Table 1. Design parameter values defined in figure 5.

Parameters	Values
$A\,(L \times L)$	6.7×6.7 mm^2
D_1	140 μm
D_2	490 μm
W_S	300 μm
W_E	16.7 μm
k	0.6 (N m^{-1})

As shown in figure 2, there are two gaps between the tri-electrode electrodes to consider, one between the intermediate electrode and MEMS (D_1), and the other between the intermediate and the primary electrodes (D_2). According to [33], which only considered air gap in the region between the fixed electrodes, the ratio of the D_2 to D_1 should always be larger than 1 to have a considerable reduction in controlling voltage. It was previously shown that the controlling voltage tends to increase with increasing relative permittivity of the spacer material between intermediate and primary electrodes. However, this can be mitigated by increasing using a thicker spacer material and so giving a larger D_2/D_1 ratio. Therefore, while air might be the best spacer material ($\varepsilon_r = 1$) in terms of voltage reduction, the additional challenges in fabrication due to having a hollow space between the electrodes may make a solid material preferable.

In order to simplify the fabrication of the experimental demonstrator, a solid quartz substrate was used between the intermediate and primary electrodes. To compensate for the possible loss in voltage reduction performance, a larger D_2/D_1 ratio was used. The performance as a function of W_S to W_E ratio was explored, to determine the lowest controlling voltage and largest deflection range enhancement before snap-down. Numerical simulations were performed to find the optimized design as described in the following section.

The schematic of the tri-electrode layers is shown in figure 4. The actuator consists of two parts which were attached together post fabrication. The layers were placed upon each other and anchored in place for experimental testing.

2.2. Tri-electrode design parameters and simulation

The designed tri-electrode is depicted in figure 5, and its parameter values are summarized in table 1. The parameters are extracted from the FEM simulations [33] and are basically according to the performance of the tri-electrode actuator. The designed parameter's values are decided based on the available materials, power supplies, and microfabrication limitations. The MEMS electrode is a large 6.7×6.7 mm^2. The

large dimensions were selected to facilitate the experimental measurement of device movement. The free space between the MEMS and the intermediate electrodes is $D_1 = 140$ μm, and the space between the intermediate and the primary electrode is $D_2 = 490$ μm. The D_2 height was selected based on the thickness of the available quartz wafer, and the D_1 height was selected to be about 100–150 μm according to the previous results of [36] which found that having D_2 almost 4–5 times D_1 gives the best performance when there is a solid material such as quartz between intermediate and primary electrodes.

The quartz substrate between intermediate and primary electrodes has a relative permittivity of 3.82. To find the intermediate electrode parameter values, FEM and RSFM were utilized to find the intermediate gap spacing (W_S), electrode width (W_E), and primary electrode voltage (V_P) that provided the best device performance. The simulations were performed in 2D mode for a unit-cell to reduce the time and increase the accuracy of the calculations. This also helped to enable smaller mesh sizes in the FEM simulations to provide smaller tolerance errors, while reducing computation time.

The unit cell is displayed in figure 5, along with the meshing, potential, and electric field distribution between electrodes.

Three modes are defined for the tri-electrode operation based on the power supply used to control the actuator. Unipolar mode is when a power supply with the same polarity (positive or negative) is used to supply the intermediate and primary electrodes. For the unipolar mode in this paper, the controlling voltage is positive. Bipolar mode is when a bipolar power supply is used, and the controlling voltage varies from negative to positive. For both these modes of operation, in order to show the voltage reduction, a figure of merit (FOM) was defined for the deflection per unit controlling voltage, and contrasted this to that of a conventional actuator:

$$\text{FOM}_S = X_{\text{snap-down}}/V_{\text{snap-down}} \tag{1}$$

$$\Delta d_u = \Delta d_b = X_{\text{snap-down}} \tag{2}$$

$$\text{FOM}_u = \Delta d_u/\Delta V_u \tag{3}$$

$$\text{FOM}_b = \Delta d_b/\Delta V_b \tag{4}$$

where $X_{\text{snap-down}}$ is the maximum deflection of the conventional actuator before snap-down, $V_{\text{snap-down}}$ is the voltage at which this occurs, FOM_S defines the figure of merit for the conventional actuator (displacement vs. voltage), Δd_u is the displacement in unipolar mode to give the movement of $X_{\text{snap-down}}$, Δd_b is the displacement in bipolar mode to give the movement of $X_{\text{snap-down}}$, FOM_u defines the figure of merit for the unipolar mode of operation occurring at voltage ΔV_u, FOM_b defines the figure of merit for the bipolar mode of operation occurring at voltage ΔV_b. All three modes along with the conventional topology are illustrated in figure 6. The displacement (*y*-axis) is common for the conventional, unipolar, and bipolar modes. The required controlling voltage (*x*-axis) is shown with the width of the green region. As can be seen, the width of the green region is smaller from conventional for the unipolar and bipolar modes, which illustrates the smaller required controlling voltage in unipolar and bipolar with respect to conventional. The green region that the controlling voltage is entirely positive in unipolar mode, and that the bipolar power supply has equal positive and negative controlling voltage. The maximum displacement mode shows a higher controllable displacement possible, and it has non-equal negative to positive voltage range.

In the maximum displacement mode, a bipolar power supply is used, but the deflection is the maximum range the actuator can travel before snap-down. This mode shows the enhancement in the controllable deflection range that is possible with the tri-electrode topology, while the other two modes show the control voltage reduction.

The voltage and deflection range of all three modes are illustrated in figure 7 for the actuator defined in table 1. The contrasting conventional actuator parameters (*A*, D_1 and *k*) are as the same values as for the tri-electrode. The FOM_S of the conventional topology at the full snap-down displacement of $X_{\text{snap-down}}$ is calculated to be $\text{FOM}_S = 1.3\ \mu\text{m/V}$. For unipolar
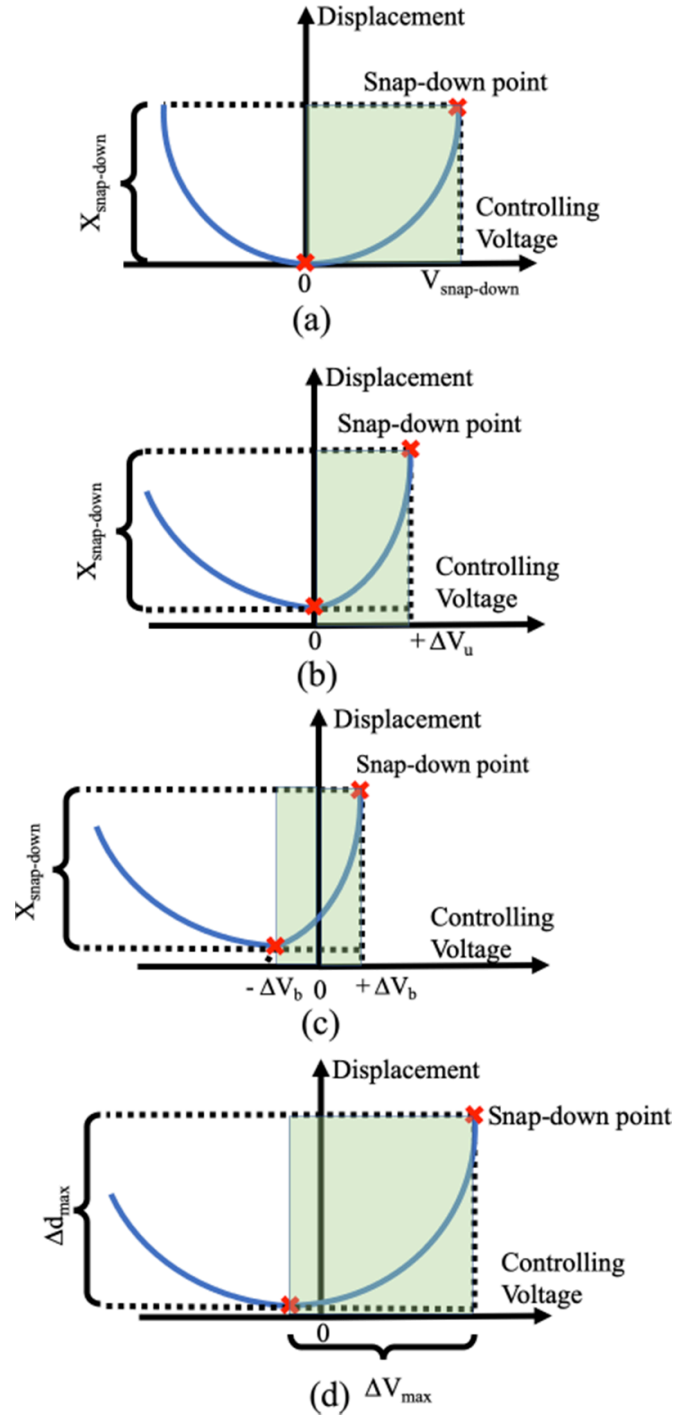

Figure 6. Three modes of unipolar (b), bipolar (c), and maximum displacement (d) in comparison with the conventional topology (a). The green region shows the controlling voltage for each of the modes.

operation, simulations show that the same $X_{\text{snap-down}}$ displacement is possible with $\text{FOM}_u = 1.4\ \text{FOM}_S$, which means the unipolar controlling voltage is 40% smaller than for the conventional actuator for the same displacement. For bipolar operation, the same $X_{\text{snap-down}}$ displacement is possible with $\text{FOM}_b = 2.6\ \text{FOM}_S$, illustrating its 2.6 times smaller required controlling voltage.
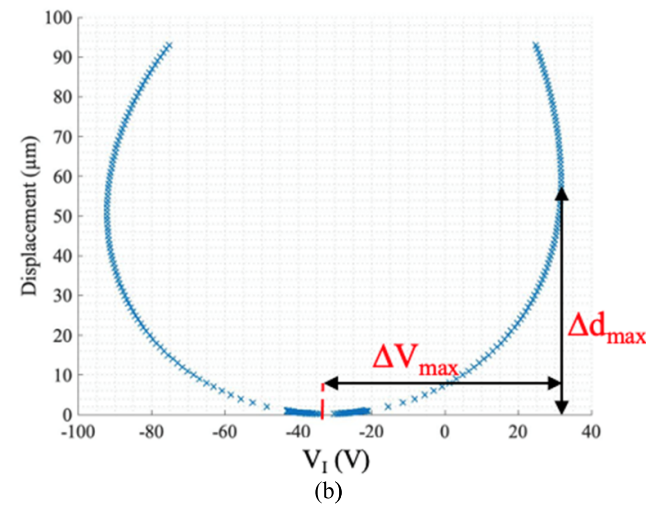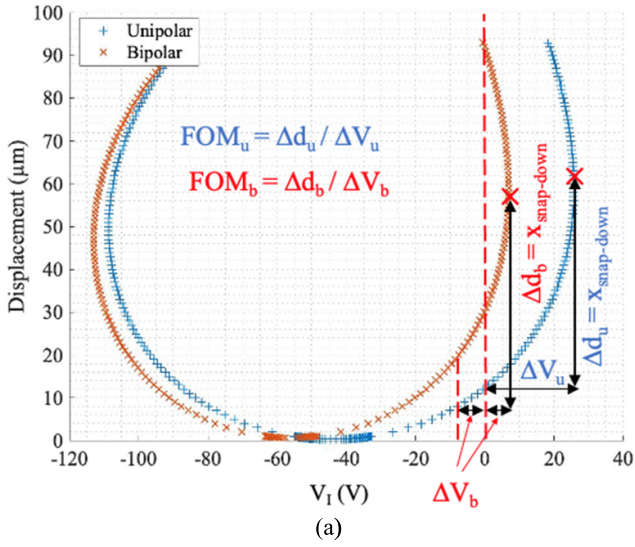
5

(a)

(b)

Figure 7. Displacement vs. V_I for (a) unipolar and bipolar modes, and (b) maximum displacement, for $D_1 = 140 \ \mu$m, $D_2 = 490 \ \mu$m, $W_S = 300 \ \mu$m, $W_E = 16.7 \ \mu$m and spring constant $k = 0.6$ N m^{-1}.

Figure 8. Displacement (Δd_u, Δd_b and Δd_{max}) vs. V_P for unipolar, bipolar, and maximum displacement modes.

Figure 9. Fabrication process steps of the MEMS moving electrode coated with aluminum as the metal electrode. (a) Thermal oxidation in furnace at 1100 °C. (b) Etching exposed open window oxide with buffer oxide etchant (BOE). (c) Silicon isotropic etch using KOH etchant and removing remaining oxide with BOE. (d) Coating the frontside of the substrate with aluminum using sputtering. (e) Etching the aluminum using aluminum etchant at 60 °C. (f) Releasing the device using RIE plasma etch.

The tri-electrode device performance is very dependent on the primary electrode voltage. For the results of figure 7, the primary electrode voltage was $V_{Pu} = 109$ V for the unipolar mode, $V_{Pb} = 140$ V for the bipolar mode, and $V_{Pmax} = 80$ V for the maximum displacement mode. These voltage values are the ones for which the best performance was found. In order to determine these voltages, the study of figure 8 was done, which shows the largest deflection possible before snap-down for the unipolar, bipolar, and maximum displacement modes, as a function of V_P.

3. Experimental testing

The experimental demonstrator consists of two parts. The upper part is the single crystal silicon MEMS moving electrode, and the lower part is the quartz material with the aluminum intermediate and primary electrodes coated on either side. The thickness of the quartz is then the spacing D_2. The
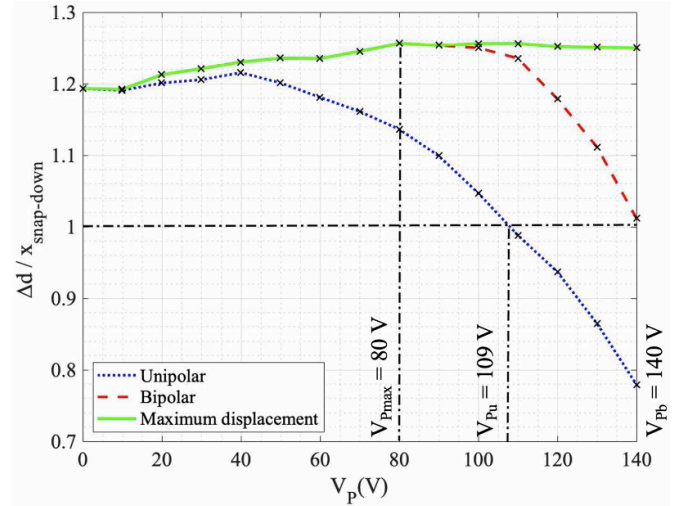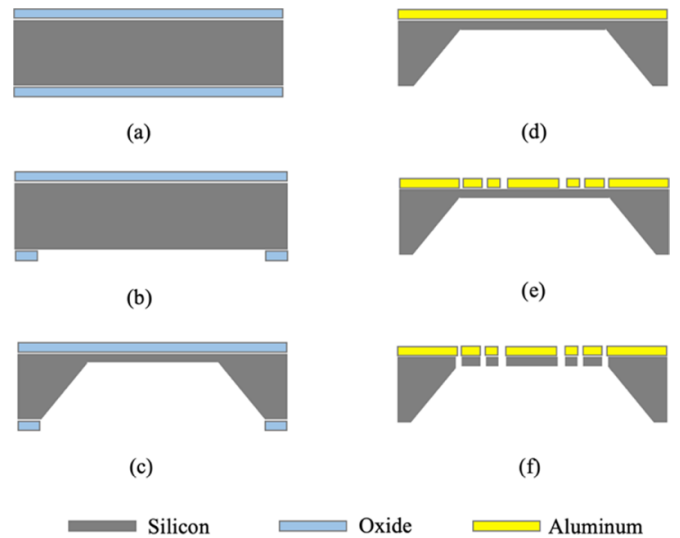
two fabricated parts are then placed upon each other to form the entire tri-electrode actuator.

3.1. MEMS fabrication process

Figure 9 shows the fabrication steps of the MEMS moving electrode. The moving electrode is formed from a 300 μm double-sided polished single crystal silicon wafer with <100> crystal orientation.

First, the wafer was cleaned using piranha etch with a combination of 1100 ml H_2SO_4 and 300 ml H_2O_2 for 10 min. Then the silicon wafer was cut into pieces using a wafer saw

Table 2. Plasma etch recipe utilized to release the MEMS moving electrode. In this recipe the etch rate is 1.1 μm min^{-1}.

Parameter	Value
Pressure	50 (Torr)
Inductively coupled plasma power	100 (Watt)
RIE power	50 (Watt)
CHF$_3$ flow	15 (SCCM)
SF$_6$ flow	30 (SCCM)
O$_2$ flow	15 (SCCM)
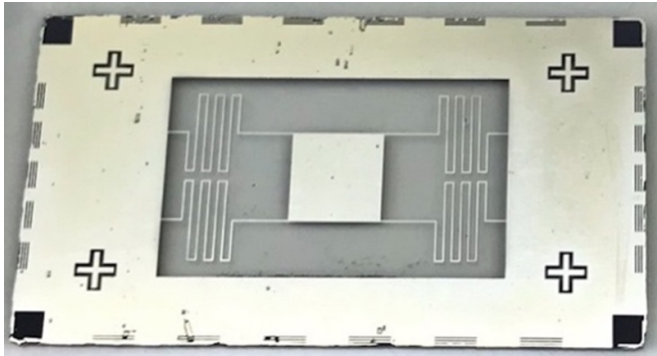
Figure 10. Fabricated MEMS electrode.

and put in a high-temperature oxidation furnace for 24 h at 1100 °C. The wet thermal oxide was grown on both sides of the samples with a thickness of 2.5 μm (figure 9(a)). The oxide is the mask layer for the following back etch step to thin the silicon wafer to the required thickness. In the next step, both sides of the sample were coated with positive HPR 504 photoresists, and the backside was patterned using photolithography. Following this, the backside thermal oxide was etched and patterned using (10:1) buffered oxide etchant (BOE) to expose the silicon area for thinning (figure 9(b)). Next, the silicon was etched in 30% KOH etchant at 80 °C with magnetic stirring of 255 rpm (figure 9(c)). The KOH etching step is performed in several steps to control the etched thickness precisely and uniformly. The silicon cavity formed by KOH etch is considered as the D_1 gap spacing for the tri-electrode. After removing the remaining oxide, 300 nm aluminum was deposited using sputtering on the frontside of the sample and patterned using photolithography (figure 9(d)). In the next step, the aluminum was etched using aluminum wet etch at 60 °C (figure 9(e)). The aluminum layer will serve as an electrode and etch protecting mask layer for the following plasma etch step. The MEMS electrode was then released with plasma etch using fluorine-based reactive ion etching (RIE) (figure 9(f)). The anisotropy of the plasma etch was determined mainly by the flow of SF$_6$ and O$_2$ gases [37]. The recipe of the RIE utilized for silicon etch is summarized in table 2. Figure 10 shows the fabricated MEMS electrode.

3.2. Stationary electrodes fabrication process

Figure 11 shows the fabrication steps of the stationary electrodes. A 490 μm single-sided polished quartz wafer was
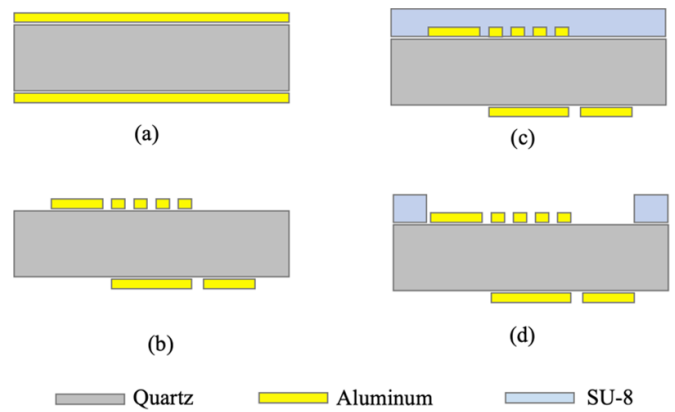
Figure 11. Fabrication process steps of stationary electrodes on quartz samples. (a) Sputtering aluminum on both sides of the quartz samples. (b) Patterning and etching aluminum with its etchant at 60 °C. (c) Spin coating SU-8. (d) Patterning SU-8.
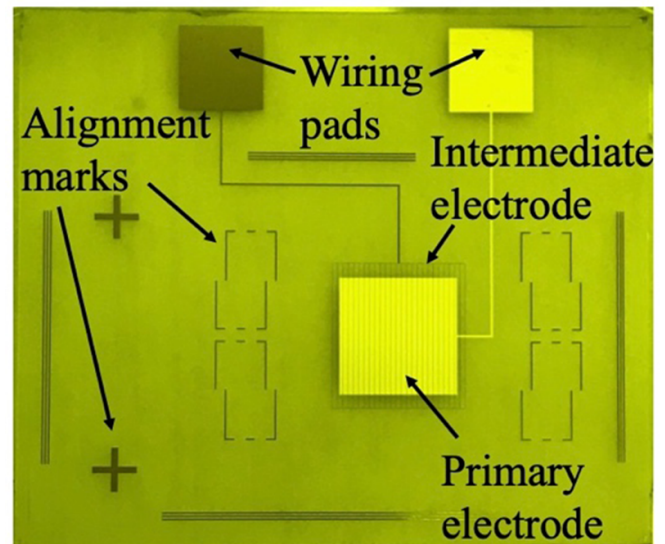
Figure 12. Fabricated intermediate (top side) and primary electrodes (backside) on quartz substrate.

cleaned using acetone and isopropyl alcohol. The thickness of the quartz sample is equal to the D_2 gap size designed in the tri-electrode topology. After cutting the wafer using a wafer saw, both sample sides were coated with 300 nm aluminum using sputtering (figure 11(a)). The aluminum was coated with a positive HPR 504 photoresist and patterned using an aluminum etchant to form the intermediate and primary electrodes on the two opposite sides of the quartz samples (figure 11(b)). Next, hexamethyldisiloxane coating was carried out for 5 min at 150 °C to improve the adhesion of the quartz samples upon which 3 μm SU-8 is spin coated on the sample and patterned using photolithography (figures 11(c) and (d)). The SU-8 is used as a thin electrically insulating spacer to isolate the MEMS electrode part and the intermediate electrode. The quartz samples are ready to be attached to the silicon-based moving MEMS electrodes. Figure 12 shows the stationary electrodes after fabrication.
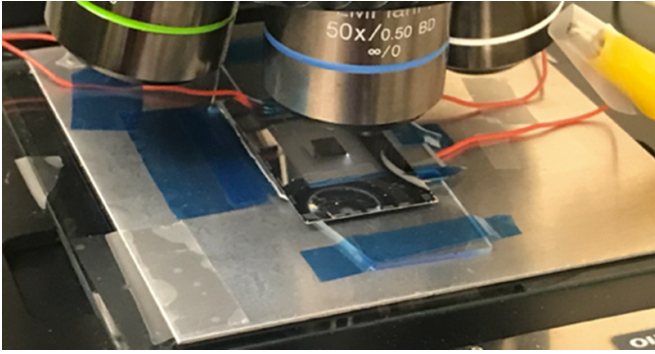
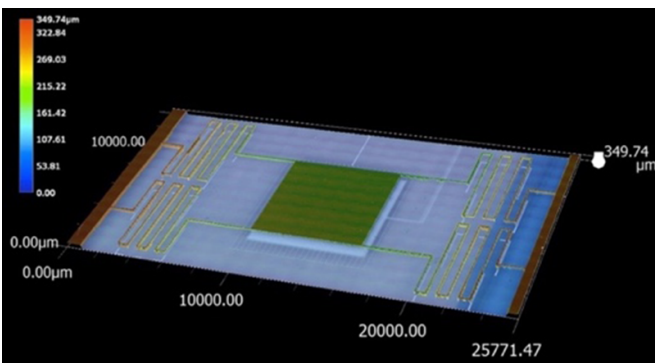**Figure 13.** Measurement set-up using Olympus microscope, showing tri-electrode device being tested.

Figure 14. The tri-electrode actuator under Keyence microscope with (500×) magnification.

Figure 15. (a) Conventional topology with D_1 gap spacing between stationary and moving electrode and (b) perforated conventional topology with D_1 gap spacing between stationary and moving electrode and W_S gap spacing between intermediate electrodes.

Figure 16. Response curve for conventional topology (blue cube curve) and perforated conventional (red star curve) when $W_S = 300\,\mu$m and $D_1 = 140\,\mu$m both simulation and measurement results.

4. Measurement results

The setup utilized for the tri-electrode test experiment is shown in figure 13. Three Agilent power supplies with different voltage ranges were employed to drive the intermediate and primary electrodes. Two were used to enable the bipolar intermediate electrode voltage (V_I), and the third was for the primary electrode voltage (V_P). Olympus (BX51) and Keyence (VHX-7100) microscopes were utilized to measure the movement of the MEMS electrode.

After attaching the two parts, the gap spacing between the moving MEMS electrode and the intermediate electrode (D_1) was measured to be $140 \pm 5\,\mu$m. Figure 14 shows the assembled device as measured by the Keyence microscope.

The tri-electrode response curve was first measured with no voltage applied to the primary electrode. In this case, the tri-electrode performs as a conventional actuator (figure 15(a)) but with a less effective stationary electrode area (figure 15(b)) due to perforation. For comparing the results with the conventional topology, the measurements were plotted along with the simulation of the conventional and perforated conventional, shown in figure 16. As was expected, the snap-down voltage for the perforated conventional actuator is larger compared to the conventional topology.

Figures 16–18 contrast the simulated performance to the experimentally tested performance of the fabricated conventional and tri-electrode actuators. Each figure has two curves,
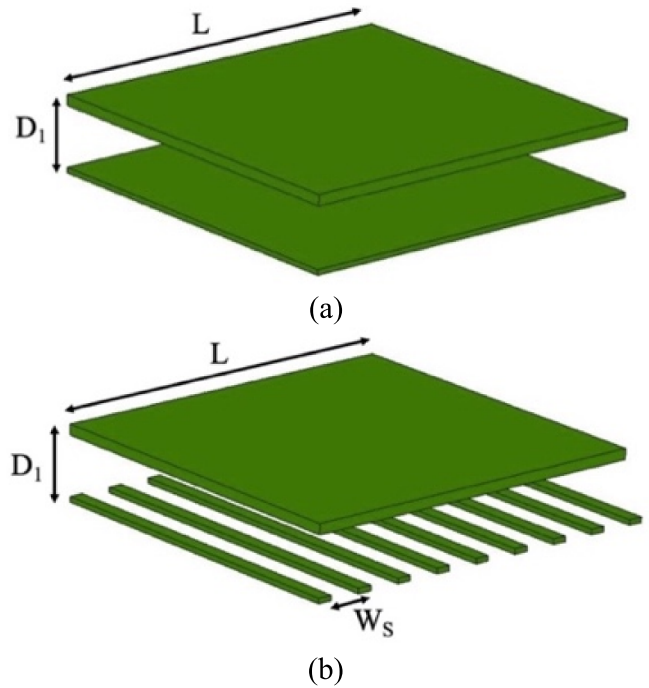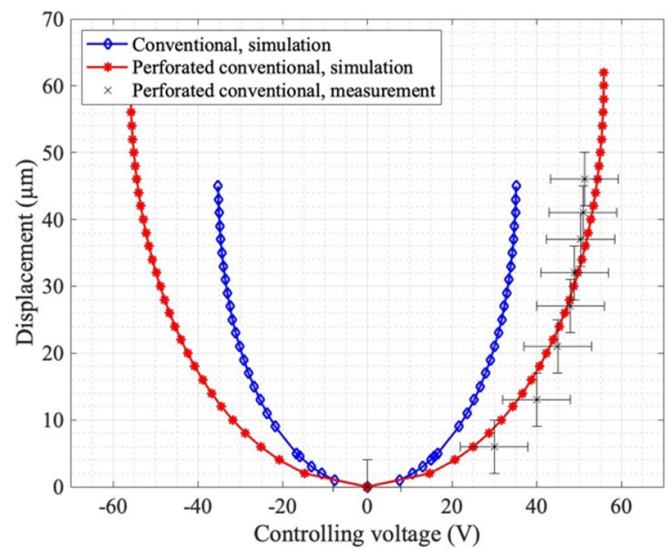
with the red star solid line showing the simulation values, and the black cross points showing the measurement results. As simulated using FEM analysis for best performance, the unipolar mode was tested with $V_{Pu} = 109$ V. The controlling voltage (V_I) was swept from 0 to 26.6 V. Figure 17(a) shows the measured displacements. It can be seen that the measurement and simulation results are in close agreement.
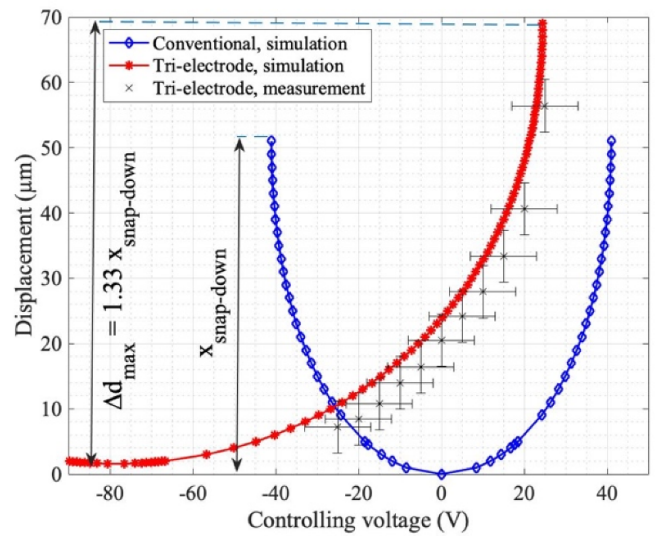
(a)
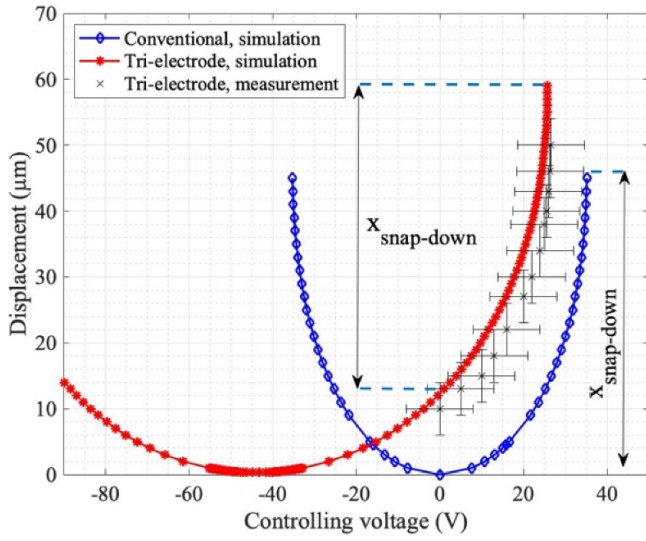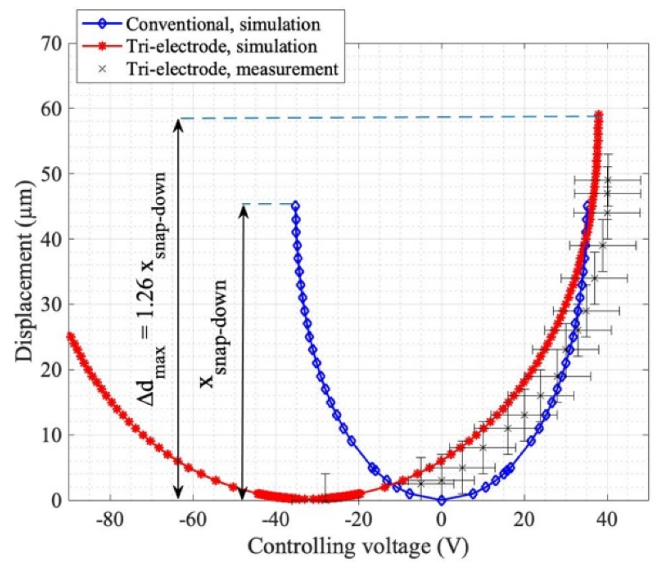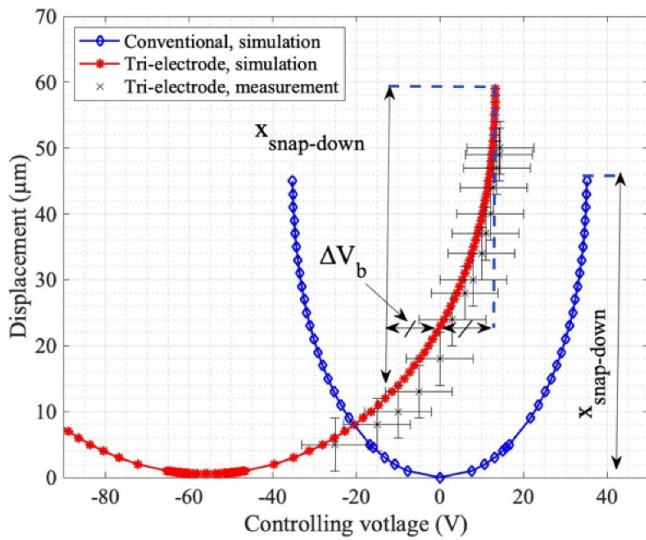
(b)

Figure 17. Displacement vs. controlling voltage measurement. (a) Unipolar tri-electrode mode with $V_{Pu} = 109$ V. (b) Bipolar tri-electrode mode with $V_{Pb} = 140$ V.

(a)

(b)

Figure 18. Displacement vs. V_I for the maximum displacement mode for when (a) $W_S = 300\ \mu$m, $D_1 = 140\ \mu$m, $V_P = 80$ V and (b) $W_S = 450\ \mu$m, $D_1 = 155\ \mu$m, $V_P = 120$ V.

In a similar fashion, the bipolar operation mode was tested by sweeping the controlling voltage from -25 to 14.5 V, with primary voltage $V_{Pb} = 140$ V. The measured results for the bipolar mode are depicted in figure 17(b). Again, close agreement between measured and simulation results is seen. Comparing both the unipolar and bipolar modes with the conventional response curve, it can be seen that the controlling voltage is smaller for the same deflection range for both.

In unipolar operation (figure 17(a)) the controlling voltage of 25.8 V gives the same displacement as the conventional actuator with 35.2 V. For the bipolar operation, only $\pm13.35\ V$ was needed. The reduction of controlling voltage magnitude is apparent in both modes, and the calculated FOM is almost equal to $\mathrm{FOM_u} = 1.4\ \mathrm{FOM_S}$ and $\mathrm{FOM_b} = 2.6\ \mathrm{FOM_S}$.

The maximum controllable displacement mode was then explored. The case for an intermediate electrode with $W_S = 300\ \mu$m and $D_1 = 140\ \mu$m is illustrated in figure 18(a). It can be seen that $\Delta d_{max} = 59\ \mu$m (for $V_P = 80$ V), which is almost 26% higher than the conventional snap-down displacement of $X_{snap\text{-}down} = 47\ \mu$m. Since the maximum displacement is also a function of the gap spacing of the intermediate electrode (W_S), another gap spacing was explored. A second intermediate electrode was fabricated with a larger gap spacing of $W_S = 450\ \mu$m, to show the impact of W_S on the tri-electrode maximum deflection range. This device had a slightly higher $D_1 = 155\ \mu$m. The result shown in figure 18(b), has $\Delta d_{max} = 69\ \mu$m (for $V_P = 120$ V), which is 33% higher than the conventional snap-down displacement of approximately $X_{snap\text{-}down} = 52\ \mu$m

for this larger D_1 gap spacing. Therefore, the intermediate electrode gap spacing (W_S) has not only a significant impact on controlling voltage reduction, but it can also be selected such to provide the actuator with a higher maximum controllable displacement possible before snap-down.

Comparing the experimental results with other recent electrostatically actuated applications is challenging, due to the fact that device performance is specific to particular MEMS design configurations. Nonetheless, some examples are given below to illustrate how the tri-electrode configuration can enable lower controlling voltages. For example, we can see in figure 17(a) that in the unipolar mode, the tested tri-actuator travels around 50 μm with only 0–26.6 V of controlling voltage. By contrast, in [31] an average of 0–221 V is required for closing and opening a microfluidic channel with a depth of not more than 9.1 μm. In [32], a controlling voltage of 0–128 V was used to control the electrostatic actuator with serpentine springs for a range of 9.89 μm. In [16], an electrostatically DM was deflected 15 μm with around 0–375 V. Therefore, we see that the tri-electrode offers a controlling lower voltage. In addition, considering the bipolar mode, the actuator can be controlled with a smaller bipolar power supply for the same displacement range.

5. Conclusions

In this work, experimental testing of a tri-electrode electrostatic actuator was undertaken to demonstrate its lower controlling voltage and enhanced deflection, compared to a conventional parallel plate electrostatic actuator. FEM simulations were used to determine optimal designs for performance improvements. Experimental measurements showed close agreement with numerical simulations. Tri-electrode designs demonstrated almost 36% reduction in controlling voltage in the unipolar mode, and 2.6 times reduction in bipolar mode, compared to the conventional topology. A maximum controllable deflection range of 33% higher than the conventional topology was experimentally demonstrated with the appropriate design of tri-electrode topology parameters. It was shown in simulations and experiments that the intermediate electrode gap spacing (W_S) has a significant effect on controlling voltage reduction and the maximum possible deflection range.

Data availability statement

The data that support the findings of this study are available upon reasonable request from the authors.

Acknowledgments

ORCID iDs

Mehdi Allameh https://orcid.org/0000-0001-8936-4131
Yu Zhou https://orcid.org/0000-0002-3405-5531
Byoungyoul Park https://orcid.org/0000-0003-4493-8343

References

[1] Roddier F 1999 *Adaptive Optics for Astronomy* (Cambridge: Cambridge University Press)
[2] Davis R and Kasper M 2012 Adaptive optics for astronomy *Annu. Rev. Astron. Astrophys.* **50** 081811–125447
[3] Booth M J 2007 Adaptive optics in microscopy *Phil. Trans. R. Soc.* A **365** 2829–43
[4] Porter J, Queener H M, Lin J E, Thorn K and Awwal A 2005 *Adaptive Optics for Vision Science: Principles, Practices, Design, and Applications* (Hoboken: John Wiley and Sons, Inc.)
[5] Chen Y, Zhang L, Ke L, Feng K, Wang W and Liu J 2019 Optimal design of an adaptive optical system for improving the focusing capability of a high-field laser *Laser Phys.* **29** 115301
[6] Ren D Q, Zhang T Y and Wang G 2021 A low-cost and high-performance technique for adaptive optics static wavefront correction *Res. Astron. Astrophys.* **21** 181
[7] Babcock H W 1953 The possibility of compensating astronomical seeing *Publ. Astron. Soc. Pac.* **65** 229
[8] Bifano T 2011 MEMS deformable mirrors *Nat. Photon.* **5** 21–23
[9] Geary J M 1995 *Introduction to Wavefront Sensors* (Bellingham: SPIE Optical Engineering Press)
[10] Helmbrecht M A, Kempf C and Rhodes P 2009 Scaling up of the Iris AO segmented DM technology for atmospheric correction *Proc. 10th Adv. Maui Opt. Space Surveillance Technol. Conf.*
[11] Bifano T G, Perreault J A, Bierden P A and Dimas C E 2002 Micromachined deformable mirrors for adaptive optics *Int. Symp. on Optical Science and Technology*
[12] Tyson R K 1991 *Principles of Adaptive Optics* (San Diego: Academic)
[13] Rukosuev A L, Belousov V N, Niktin A N, Sheldakov Y V, Kudryashov A V, Bogachev V A, Volkov M V, Garanin S G and Starikov F A 2020 Smart adaptive optical systems for correcting the laser wavefront distorted by atmospheric turbulence *Quantum Electron.* **50** 707
[14] Bowens-Rubin R, Hinz P, Jonker W, Kuiper S, Laguna C and Maniscalco M 2020 Performance of large-format deformable mirrors constructed with TNO variable reluctance actuators *Proc. SPIE* **11448** 114485
[15] Zhang Y and Roorda A 2006 MEMS deformable mirror for ophthalmic imaging *Proc. SPIE* **6113** 61130
[16] Banerjee K, Rajaeipour P, Zappe H and Ataman C A 2019 37-actuator polyimide deformable mirror with electrostatic actuation for adaptive optics microscopy *J. Micromech. Microeng.* **29** 085005
[17] Madec P Y 2012 Overview of deformable mirror technology for adaptive optics and astronomy *Proc. SPIE* **8447** 844705
[18] Bifano T G, Perreault J, Krishnanmoorthy Mali R and Horenstein M N 1999 Micromechanical deformable mirrors *IEEE J. Sel. Top. Quantum Electron.* **5** 83–89
[19] Xu X-H, Li B-Q, Feng Y and Chu R-J 2007 Design, fabrication and characterization of a bilk-PZT-actuated MEMS deformable mirror *J. Micromech. Microeng.* **17** 2439
[20] Lin P-Y, Hsieh H-T and John Su G-D 2011 Design and fabrication of a large-stroke MEMS deformable mirror for wavefront control *J. Opt.* **13** 055404

[21] Dagel D J, Cowan W D, Spahn O B, Grossetete G D, Grine A J, Shaw M J, Resnick P J and Jokiel B 2006 Large-stroke MEMS deformable mirrors for adaptive optics *IEEE/ASME J. Microelectromech. Syst.* **15** 572–83

[22] Hamelinck R F M M 2010 Adaptive deformable mirror: based on electromagnetic actuators *PhD Thesis* Eindhoven University of Technology

[23] Pamidighantam S, Puers R, Baert K and Tilmans H A C 2002 Pull-in voltage analysis of electrostatically actuated beam structures with fixed-fixed and fixed-free end conditions *J. Micromech. Microeng.* **12** 458

[24] Chiou J C and Lin Y J 2005 A novel large displacement electrostatic actuator: pre-stress comb-drive actuator *J. Micromech. Microeng.* **15** 1641

[25] Chu C-H, Shih W-P, Chung S-Y, Tsai H-C, Shing T-K and Chang P-Z 2007 A low actuation voltage electrostatic actuator for RF MEMS switch applications *J. Micromech. Microeng.* **17** 1649

[26] Hung E S and Senturia S D 1999 Extending the travel range of analog-tuned electrostatic actuators *J. Microelectromech. Syst.* **8** 497–505

[27] Daeichin M, Miles R N and Towfighian S 2020 Large-stroke capacitive MEMS accelerometer without pull-in *IEEE J. Microelectromech. Syst.* **21** 3097–106

[28] Lee K B 2007 Non-contact electrostatic microactuator using slit structures: theory and a preliminary test *J. Micromech. Microeng.* **17** 2186

[29] Su J, Yang H, Fay P, Porod W and Bernstein G H 2010 A surface micromachined offset-drive method to extend the electrostatic travel range *J. Micromech. Microeng.* **20** 015004

[30] Rosa A M, Bruyker D D, Volkel A R, Peeters E and Dunec J 2004 A novel external electrode configuration for the electrostatic actuation of MEMS based devices *J. Micromech. Microeng.* **14** 446

[31] Atik A C, Ozkan M D, Ozgur E, Kulah H and Yildirim E 2020 Modeling and fabrication of electrostatically actuated diaphragm for on-chip valving of MEMS-compatible microfluidic systems *Micromech. Microeng.* **30** 115001

[32] Admassu D, Durowade T, Velicu S, Sivananthan S and Gao W 2020 Estimation of the mechanical stiffness constant of MEMS-based parallel-plate micro-actuators *Microsyst. Tech.* **27** 2751–9

[33] Allameh M and Shafai C 2021 Tri-electrode MEMS electrostatic actuator with lower control voltage and higher stroke for actuator array implementations *J. Electrost.* **114** 103635

[34] Allameh M, Park B and Shafai C 2022 Enhanced travel range bipolar tri-electrode electrostatic actuator using extended background electrode *Proc. SPIE* **12013** 143–9

[35] Seeger J I and Cray S B 1997 Stabilization of electrostatically actuated mechanical devices *Proc. of Int. Solid State Sensors and Actuators Conf.*

[36] Allameh M, Park B and Shafai C 2022 Performance study of MEMS tri-electrode electrostatic actuator with glass and SU-8 between intermediate and primary electrodes *MNE Eurosensors 2022 Conf.*

[37] Zhou Y 2012 Investigation of a micromachined electric field mill to maximize the electrostatic field sensitivity *MSc Thesis* University of Manitoba